Crystallographic characterization of U<inf>2</inf>CrN<inf>3</inf>: A neutron diffraction and transmission electron microscopy approach

Nuclear Materials and Energy 35 (2023) 101441

Contents lists available at ScienceDirect

Nuclear Materials and Energy

journal homepage: www.elsevier.com/locate/nme

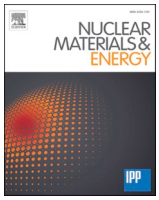

Crystallographic characterization of U_2CrN_3: A neutron diffraction and transmission electron microscopy approach

Sobhan Patnaik [a,*,1], Yulia Mishchenko [a,1], Jennifer H. Stansby [b], Andrea Fazi [c], Vanessa K. Peterson [d], Daniel Jädernäs [e], Mattias Thuvander [c], Kyle D. Johnson [e], Edward G. Obbard [b], Denise A. Lopes [a,f]

[a] KTH Royal Institute of Technology, Stockholm, Sweden
[b] University of New South Wales, Sydney, Australia
[c] Chalmers University of Technology, Göteborg, Sweden
[d] Australian Nuclear Science and Technology Organization, Lucas Heights, Australia
[e] Studsvik Nuclear AB, Nyköping, Sweden
[f] Westinghouse Electric Sweden AB, Västerås, Sweden

A B S T R A C T

In this study, neutron diffraction and transmission electron microscopy (TEM) have been implemented to study the crystallographic structure of the ternary phase U_2CrN_3 from pellet to nano scale respectively. Recently microstructural evaluation of this ternary phase has been performed for the first time in pellet condition, overcoming the Cr evaporation issue during the conventional sintering process. In this work for the first time, the crystallographic structure of the ordered ternary U_2CrN_3 phase, stabilized in pellet condition, has been obtained by implementing neutron diffraction. For this study, pellets of the composite material UN with 20 vol % CrN were fabricated by powder metallurgy by mixing UN and CrN powders followed by Spark Plasma Sintering (SPS). TEM was used to investigate the nanoscale structure with a thin lamella of the order of 100–140 nm produced by focused ion beam (FIB). The neutron data revealed the phase composition of the pellet to be primarily 54(8) wt.% U_2CrN_3, in good agreement with the stoichiometry of starting reagents (UN and CrN powder) and metallographic analysis. Neutron data analysis confirms that all the crystallographic sites in U_2CrN_3 phase are fully occupied reinforcing the fully stoichiometric composition of this phase, however, the position of the N at the *4i* site was found to be closer to the Cr than previously thought. TEM and selected area electron diffraction rendered nano-level information and revealed the presence of nano domains along grain boundaries of UN and U_2CrN_3, indicating a formation mechanism of the ternary phase, where the phase likely nucleates as nano domains in UN grains from migration of Cr.

Introduction

Advances in nuclear materials lead to improvements in the safety and sustainability of nuclear energy, which provides 10% of global electricity and is the largest source of low-carbon power in advanced economies [1]. To achieve higher burn-up and increased fuel cycle time, uranium mononitride (UN) and UN composites with a higher uranium density than the current benchmark, UO_2, are being considered under the Accident Tolerant Fuel (ATF) initiative [2]. Given that the oxidation resistance of UN is inferior to that of UO_2, there is a drive to explore UN composites which contain additives to improve corrosion/degradation resistance to mitigate serious issues in the event of a fuel rod failure. UN mixed with several additives such as AlN, ZrN, and CrN have been studied [3]. Some of these additives resulted in full phase segregation, such as AlN, while others formed complete solutions, such as ZrN. In both these cases no significant change in the UN crystal structure was observed. Incorporation of Cr and CrN with UN results in the formation of a new stoichiometric ternary phase U_2CrN_3 (space group *Immm*), which is an orthorhombic distortion of the cubic UN crystal lattice (space group $Fm\bar{3}m$). Recently, the ternary phase U_2CrN_3 was stabilized during sintering of the UN-CrN composite in pellet form [3]. The stabilization of this ternary phase in pellet configuration was demonstrated to be tricky above 1600 °C due to Cr evaporation in conventional sintering [4]. The microstructural and crystallographic analyses of the stable ternary phase in pellet form synthesized by Spark Plasma Sintering (SPS) [3] was investigated using scanning electron microscopy (SEM) with standardized energy dispersive spectroscopy (EDS) and electron backscatter diffraction (EBSD) techniques [5]. Although EBSD has enabled the local evaluation of different surface regions of such samples previously, crystallographic structure in the bulk has never

* Corresponding author.
E-mail address: patnaik@kth.se (S. Patnaik).
[1] These authors contributed equally to this work.

https://doi.org/10.1016/j.nme.2023.101441
Received 29 September 2022; Received in revised form 14 April 2023; Accepted 3 May 2023
Available online 8 May 2023

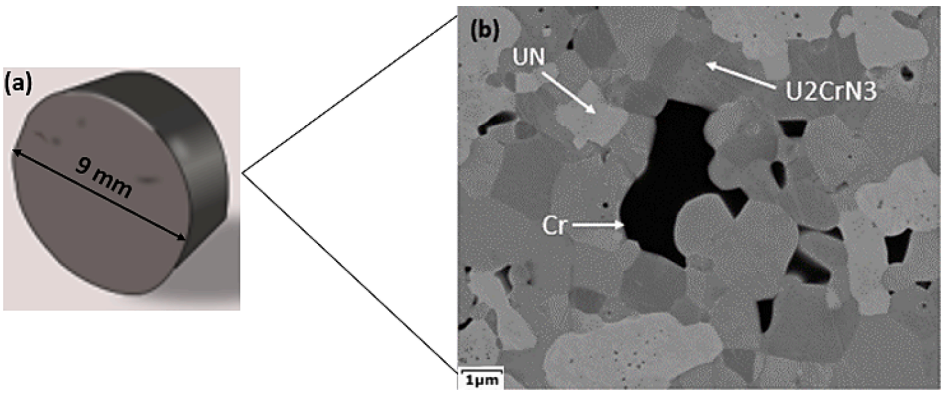

Fig. 1. (a) SPS sintered U_2CrN_3-UN pellet showing (b) microstructure and phase identifications.

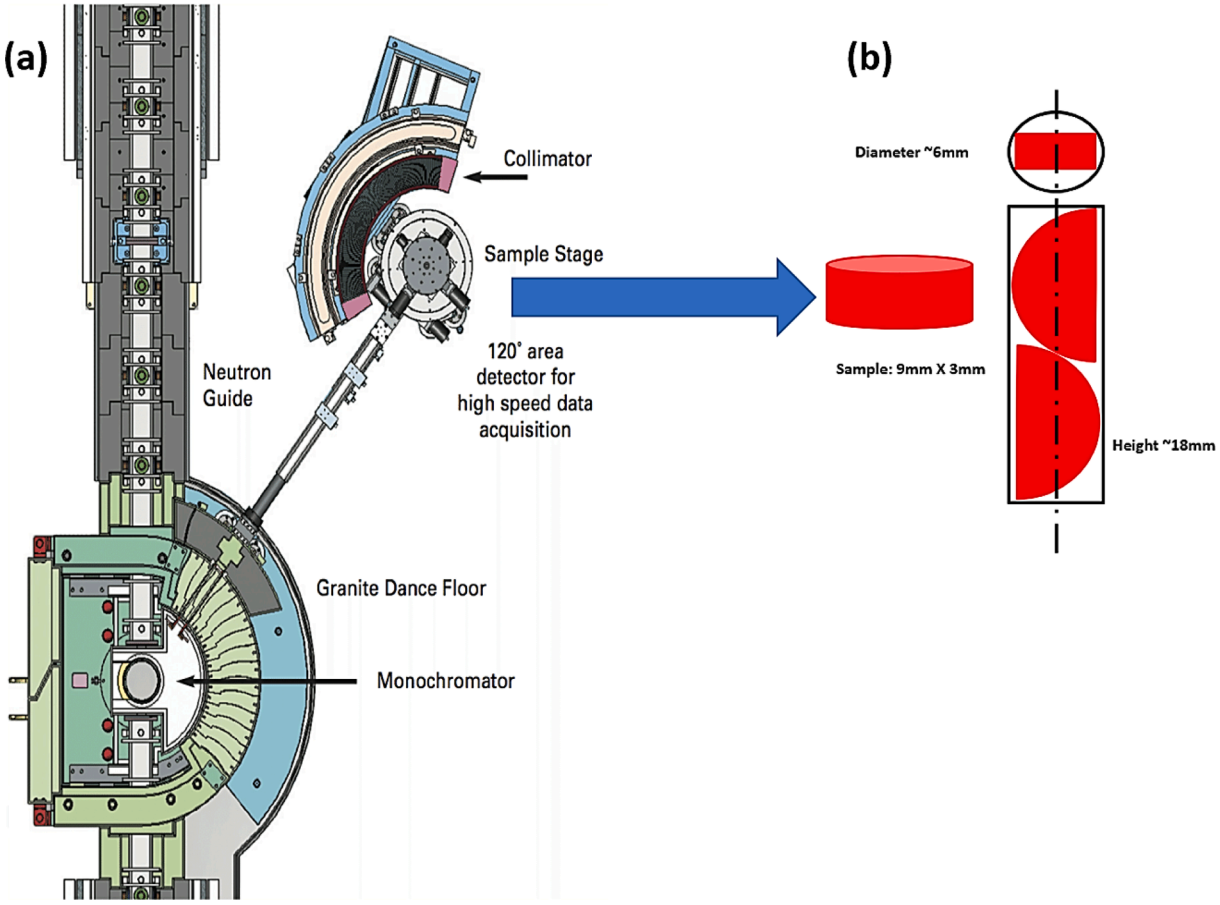

Fig. 2. Schematic of the (a) ANSTO High-Intensity Powder Diffractometer and (b) samples cut and loaded in the flanged vanadium can.

been investigated for the ternary U_2CrN_3 phase.

Crystallographic information has been reported once by Benz *et al.* using X-ray diffraction for the free flowing powder, with the structure consisting of corner-sharing CrN_4 square planar units oriented parallel to the (0 1 0) plane where the central Cr atoms sit in the cuboid of UN_7 polyhedron [6,7]. This work established two crystallographically distinct sites for octahedrally coordinated N: N1 at *2b* sites that bridge Cr atoms and neighbor 4 U atoms in the (1 0 0) plane, and N2 at 4*i* sites connecting Cr and U atoms along the c axis which is surrounded by 4 U atoms in the (0 0 1) plane as shown in Fig. A1 of Appendix A. Due to a factor ~ 172 difference in the atomic scattering factor from (low Z) N compared to (high Z) U atoms using X-ray radiation, the N coordinates were not determined experimentally. Information regarding atomic coordinates is contained within the intensities of diffraction peaks. For X-ray diffraction, the measured intensity is proportional to the square of the atomic scattering factor, f, which scales with the atomic number, Z. In the case that there is a large difference in atomic number and therefore scattering lengths, crystallographic details can only be obtained for the heavier atom. X-ray diffraction therefore does not provide full information regarding the position of these lighter elements in the material and information concerning the effect of micro-strain and crystalline size may be in doubt. However, for neutron diffraction, the scattering lengths vary independently of Z. For example, the neutron scattering lengths of U_{nat}, Cr, N are 8.417, 3.635 and 9.36 barns, respectively. Neutron diffraction can therefore be used to provide more detailed crystallographic information about the U_2CrN_3 phase, which is of

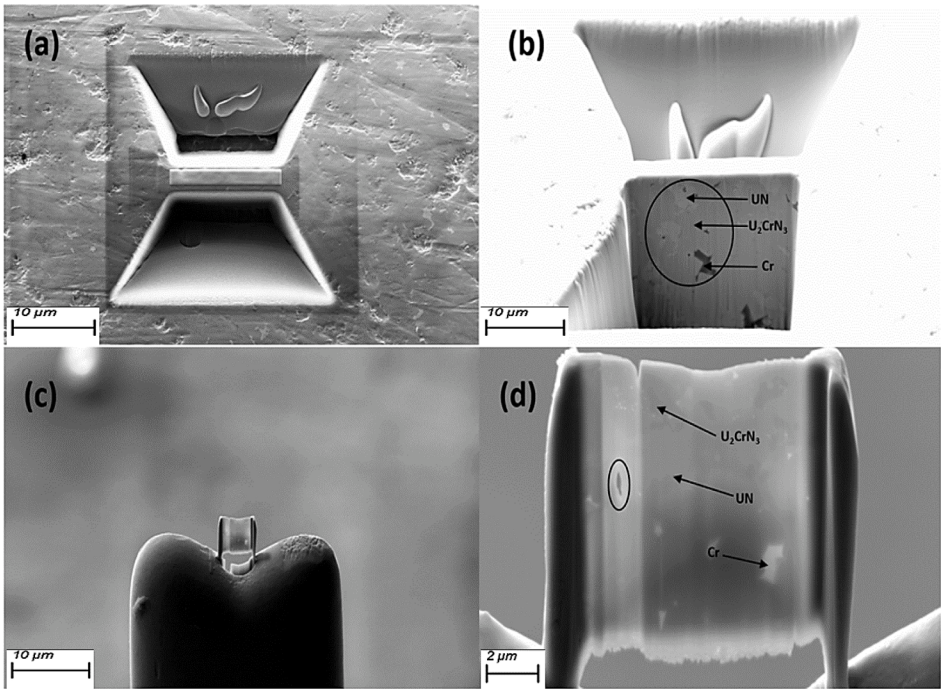

Fig. 3. (a) Trench creation by material removal in the bulk using FIB (top view); (b) SEM image (front view) of the trench showing phases (black encircled) (c) Lamella mounted on the TEM grid; (d) Thin lamella showing the three phases (slight crack can be seen within the black encircle area).

particular interest for the ATF concept. An accurate description of potential fuel candidates is fundamental to future modelling or experimental work on U_2CrN_3.

In the present work, a new crystal structural model based on neutron diffraction data is presented for U_2CrN_3. Additionally, further crystallographic structure of the isolate grains UN and U_2CrN_3 in the composite pellet was obtained via electron diffraction patterns from TEM. At higher magnifications, a formation mechanism of U_2CrN_3 can be initially proposed be retrieved, revealing that the ternary phase likely nucleates as nano domains in UN grains from migration of Cr into UN.

The continued development of prospective nuclear fuels, such as UN-CrN, requires a detailed understanding of the material crystal structure, and a detailed study from the pellet to nano level has been presented using neutron diffraction and TEM, respectively.

Methodology

Sample fabrication and characterization

The composite UN with 20 vol% CrN (UN-9.5 wt% CrN) pellets were sintered by SPS using the Dr. Sinter, 530-ET machine (Stockholm University, Department of Materials and Environmental Chemistry) from UN powder produced from hydriding-nitriding-denitriding process [8] and commercially obtained 99.99% purity CrN from Nanografi. For simplicity the UN20vol%CrN (UN-9.5 wt% CrN) pellets will be referred to as U_2CrN_3-UN on the rest of this work. X-ray diffraction (XRD) analysis performed on the CrN powder revealed the powder had mixture of 15% CrN and 85% Cr_2N by weight as previously reported by Mischenko et al. [9]. Approximately 3 g of powder (UN and CrN/Cr_2N) was used per pellet and premixed in a mortar with a pestle prior to filling the graphite sintering dies (9.3 mm inner diameter). The inside of each die was lined with thin graphite foil to prevent the interaction between the powders and the die. The temperature of the sample during sintering was measured through a tiny hole on the surface of the graphite die with a pyrometer. The pellets were sintered in an argon atmosphere under vacuum (6 to 9 Pa) at 1723 K, with a uniaxial pressure of 70 MPa and a maximum hold time of 3 min at the peak temperature. This resulted in a very high 99% dense composite U_2CrN_3-UN pellet as shown in Fig. 1. The phase composition and crystallographic orientation was characterized using SEM with standardized EDS.

Neutron diffraction analysis

Room temperature neutron diffraction data were collected on Wombat, the high-intensity diffractometer at the Open-Pool Australian Light water (OPAL) Research Reactor, located at the Australian Nuclear Science and Technology Organization (ANSTO) [10]. Two fuel pellet fragments cut in half like a semi-disk and weighing a total of 2.75 g, were sealed in a flanged vanadium can of ~ 6 mm internal diameter similar to that shown in Fig. 2 and sealed with a Swagelok VCR flange [11] before loading onto the sample stage [12].

Neutron diffraction data were collected at room temperature using a wavelength of 0.24131(3) nm, determined using the National Institute of Standards and Technology (NIST) LaB_6 660b standard reference material [13]. Data were analyzed using Rietveld refinement with the software package GSAS-II [14]. Rietveld refinement was performed using data within the momentum transfer (Q) range 12.6 $nm^{-1} \leq Q \leq$ 48.2 nm^{-1} ($Q = \frac{4\pi sin\theta}{\lambda}$, where θ = half the angle of the diffracted neutrons and λ is the neutron wavelength) with an absorption correction using the packing density of the pellet fragments in the vanadium as calculated using the NIST neutron activation and scattering calculator [15]. Noting, however, that imperfect packing of the pellets and additional unknown geometry effects means the correction is an overestimate. In the structural refinement, instrumental contributions were determined using Rietveld refinement of the obtained neutron diffraction data collected for the NIST LaB_6 660b standard reference material under the same instrument configuration as the sample pellet and fixed in the sample structure refinement. The background was modelled using a 5-term Chebyshev polynomial and sample displacements perpendicular and parallel to the neutron beam were refined.

Transmission electron microscopy

Nano-scale evaluation of the sample was performed using TEM. In

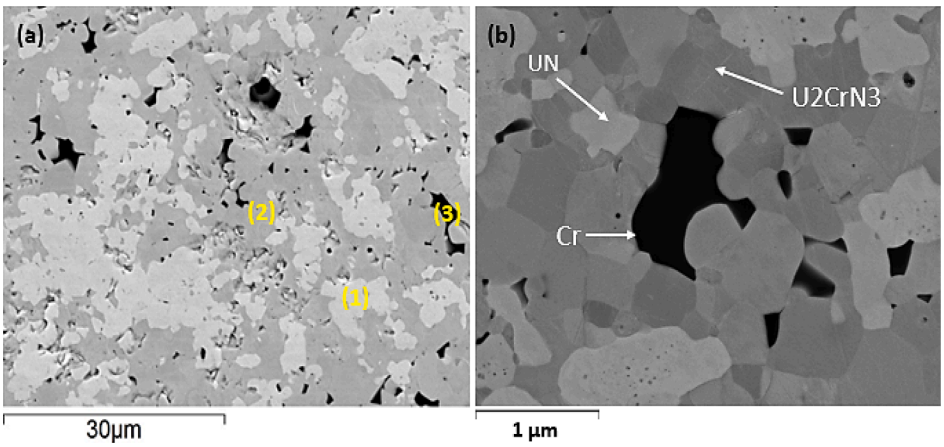

Fig. 4. (a) SEM (BSE) image of the sintered U_2CrN_3-UN pellet (b) Magnified SEM image showing the phases present in the composite microstructure.

Table 1
EDS analysis of U_2CrN_3 phase and phase fractions in U_2CrN_3-UN pellet microstructure.

Phase	Volume %	Weight %	N content (atom %)	Cr content (atom %)	U content (atom %)
U_2CrN_3	62.06 ± 2.77	60.24 ± 1.56	48.6 ± 1.3	17.8 ± 0.5	33.6 ± 1.1
UN	33.83 ± 2.76	37.47 ± 1.81	56.9 ± 0.9	–	43.1 ± 0.9
Cr	4.12 ± 0.01	2.29 ± 0.25	–	98.6 ± 0.8	–

doing so, a lamella was extracted from a Bakelite-embedded sample with a dual-beam focused ion beam/scanning electron microscopy (FIB/SEM) in a FEI Versa 3D workstation implementing standard procedures for *in-situ* sample lift-out and preparation [16]. In the preliminary stage of lamella preparation, the site of interest was identified, and protective Platinum (Pt) was electro-deposited at 5 kV, 8nA over a 2 μm × 20 μm area at a thickness of 0.2 μm, for 2 min. This process was followed by ion-beam deposition of more Pt at 30 kV, 0.3nA over the 2 μm × 20 μm at a thickness of 2 μm for 12–14 min. Thereafter, rough milling was implemented to obtain a regular cross section of the region of interest by removing material from both side at 30 kV, 50nA, for an area of 30 μm × 20 μm and maximum depth of 20 μm for 10 min on each side. Depth was decreased gradually while moving away from the region of interest. Furthermore, cleaning cross section (CCS) was done to remove the excess unwanted material from the sides of the region of interest prior to lift-out. CCS was carried out 3at 0 kV, 15nA over an area of 30 μm × 4μmat a depth of 20 μm for 7–10 min for each side. Rectangular ion milling was used to remove the material from under the lamella for extracting the volume of interest. This was achieved by making an U-shaped under cut of 3 μm thickness at 30 kV, 5nA for about 5–10 min until a thick lamella was obtained. The revealing U_2CrN_3-UN pellet microstructure is shown in Fig. 3 **(a) and 3 (b)**.

After making a thick lamella ~ 200–300 nm, a lift-off manipulator (Omniprobe) is used to extract the lamella from the bulk sample. The lamella is then fixed/glued to the needle's tip and eventually on the TEM copper half-grid by depositing Pt metal 'welding' via ion beam at 30 kV, 0.1nA for about 1–2 min. In order to make a strong welding of the lamella on the grid excess Pt metal is deposited to ensure adhesion between the lamella, needle and the grid as shown in Fig. 3 **(c)**. Thin lamella was created by back-side milling using low milling rates until a thickness of approximately 100–120 nm was achieved. At this thickness, further thinning was not possible since the lamella showed early signs of cracking, marked by black circle as can be seen in Fig. 3 **(d)**. The final thinning steps followed to obtain the thin lamella could be outlined as follows:

(a) Step 1: CCS 30 kV, 1nA, +/- 2° tilt (5 min/side)
  (i) CCS 54° tilt bottom to top.
  (ii) CCS 50° tilt bottom to top.
(b) Step 2: CCS 30 kV, 300pA +/- 1.5° tilt (thickness about 300 nm, 5–10 min/side)
(c) Step 3: CCS 30 kV, 100pA +/- 1.2° tilt: Final thickness about 100 nm (5–10 min/side).
(d) Low kV clean is always needed for crystalline material.
  (i) Rectangle 5 kV + 48pA, +/- 5; using rectangle Z = 200 nm (1–2 min/side)
  (ii) Rectangle 2 kV + 27pA, +/- 7; using rectangle Z = 30 nm (20 s/side)

Prior to conducting the TEM analysis, a combination of secondary and back scattered electron (BSE) scanning electron microscopy (SEM) was performed on the lamella to identify phases present in the microstructure as marked in Fig. 3 **(d)**. Thereafter, bright field TEM (BF-TEM) images and selected area electron diffraction patterns (SAED) data were collected on a FEI Tecnai T20 LaB6 operating at 200 keV acceleration voltage. Measurements were performed immediately after the lamella preparation to minimize the effect of sample oxidation. Simulated SAED data were calculated with JEMS Electron Microscopy Software V4.4631 using input obtained from the Materials Project database [1,17].

Results and discussion

Microstructure and phases composition

The microstructure of the composite U_2CrN_3-UN pellets is shown in Fig. 4, where three distinct phases can be identified: (1) the lightest in color matrix, (2) a dark grey phase dispersed throughout the matrix, and (3) small dark phase inclusions localized at grain boundaries [3]. High magnification micrographs were taken, one of which is presented in Fig. 4 **(b).**

A semi-quantitative chemical analysis of the composite microstructure was evaluated using standardized EDS in several different locations corresponding to the distinct phases identified in Fig. 4. Phase fractions were estimated from Fig. 4 **(a)** using ImageJ [18] with a threshold function supporting that the pellet is composed primarily of the U_2CrN_3 ternary phase. The results from standardized EDS and phase compositions of the U_2CrN_3-UN pellet have been reported in Table 1. It could be noticed that the concentration of Cr in the doped grains was always the same highlighting the very stochiometric character of this U-Cr-N system, i.e., no gradient of Cr concentration was observed through all the sample.

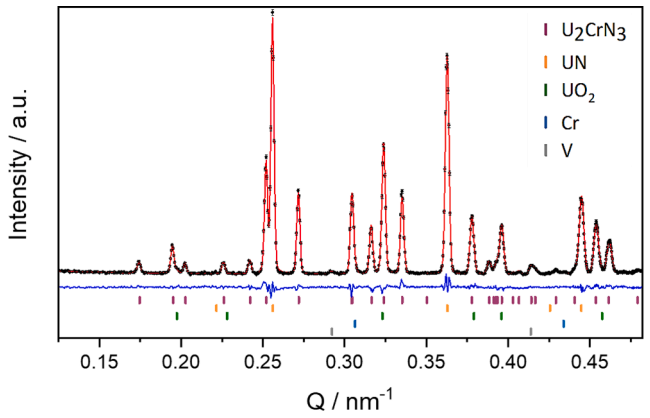

Fig. 5. Rietveld refinement profile using neutron diffraction data collected at 0.24131 nm of the pellet nominally comprised of UN-20 vol%CrN (UN-9.5 wt% CrN). The data were indexed to the phases U_2CrN_3 (space group *Immm*, 54(8) wt.%, 56.04(1) vol.%), UN (space group *Fm* $\bar{3}$ *m*, 42(7) wt.%, 38.2(1) vol.%), UO_2 (space group Fm $\bar{3}$ m, 2.1(0.4) wt.%, 2.5(0.2) vol.%), Cr (space group *Im* $\bar{3}$ *m*, 1.8(0.3) wt.%, 3.26(0.1) vol.%) and V (space group *Im* $\bar{3}$ *m*, arising from sample environment). The observed data are shown as black circles with errors bars, the calculated model as a solid red line, and the difference between the data and the model as the blue line below. Vertical markers show the positions of Bragg reflections for phases with colors as per the legend inset. (For interpretation of the references to color in this figure legend, the reader is referred to the web version of this article.)

Table 2
Crystallographic parameters for U_2CrN_3 (54(8) wt.% or 56.04(8) vol.%) as determined from Rietveld analysis of neutron diffraction data. Space group Immm, profile R-factor (R_p) = 3.39%, weighted profile R-factor (wR_p) = 4.21%, a = 0.37388(2) nm, b = 0.33194(2) nm, c = 1.23393(7) nm.

Atom type	Site label	Wyckoff	x	y	z	SOF[a]	Isotropic ADP[b] / pm^2
U	U	4*i*	0	0	0.3550 (2)	1.0	0.2(1)
Cr	Cr	2*a*	0	0	0	0.98(3)*	0.3(2)
N	N1	2*b*	0.5	0	0	1.01(1)*	0.2(1)[c]
N	N2	4*i*	0	0	0.1676 (2)	0.99(1)*	0.2(1) [c]

[a] Site occupation factor.
[b] Isotropic atomic displacement parameters (U_{iso}).
[c] Constrained to be equal.
* Fixed to 1 at final stage of refinement.

Table 3
U-N and Cr-N bond lengths determined from neutron diffraction compared to XRD.

Source	Bond	Bond Length (nm)
X-Ray	Cr-N	0.20563(3)
	U-N	0.2327(4)
Neutrons	Cr-N	0.18624(1)
	U-N	0.25284(2)

Phase crystallography by neutron diffraction

The phases presented in the composite U2CrN3-UN pellet were analyzed using neutron diffraction. Rietveld refinement profiles using the diffraction data are shown in Fig. 5. All reflections in the diffraction data could be accounted for by U_2CrN_3, UN, Cr, UO_2 and V phases (the latter arising from the sample can) and provided a good description of the data (goodness-of-fit, GOF = 1.12) – complete results are provided in Appendix A. The starting structures were obtained from the Inorganic Crystal Structure Database (ICSD) [6,7,19,20,21].

The sample pellets were found to be a mixture of 54(8) wt.% (56.04 (1) vol.%) U_2CrN_3 (space group *Immm*), 42(7) wt.% (38.2(1) vol.%) UN (space group *Fm* $\bar{3}$ *m*), 2.1(0.4) wt.% (2.5(0.2) vol.%) UO_2 (space group *Fm* $\bar{3}$ *m*) and 1.8(0.3) wt.% (3.26(0.1) vol.%) Cr metal (space group *Im* $\bar{3}$ *m*) in good agreement with SEM-EDS analysis as reported in Table 1. The portion of the U_2CrN_3 phase detected in the pellet fragments (55 wt%) is also in agreement with that expected from the nominal composition (50 wt%), where uncertainty arises from the CrN:Cr_2N ratio in the CrN powder.

The refined crystal structure parameters for the U_2CrN_3 are shown in Table 2, details of the UN, UO_2 and Cr phases are provided in Appendix B. The coordinates of atoms located on general positions were refined. For U_2CrN_3 and UN, the site occupancy of U was fixed to unity, based upon the compositions of similar phases previously reported [6,7]. While the site occupation factors (SOFs) were allowed to refine for the remaining atoms in U_2CrN_3, the results in Table 2 show that all sites are best described as being fully occupied, within error. The observed U_2CrN_3 stoichiometry validates density functional theory (DFT) calculations for the incorporation of Cr in the UN lattice, which suggested a maximum solubility of 33 atomic % Cr [3].

Isotropic atomic displacement parameters (ADPs) for each crystallographic site in the U_2CrN_3 and UN structural models were also refined. Due to the small weight fraction of the UO_2 and Cr phases in the pellet fragments, all crystallographic parameters for the UO_2 and Cr were fixed throughout the refinement.

The lattice parameter for the UN phase obtained from the neutron data (a = 0.48882(4) nm) is congruent with that reported for pure UN using X-ray powder diffraction (a = 0.48889(3) nm), confirming the absence of Cr solubility or other impurities in the UN phase [3]. The good match with UN standards demonstrates an excellent description of the instrumental parameters obtained from the LaB_6 standard and adds certainty to the updated lattice parameters reported herein for the U_2CrN_3 phase [6]. The lattice parameters obtained for the U_2CrN_3 phase from the neutron data (a = 0.37388(2) nm, b = 0.33194(2) nm, c = 1.23393(7) nm) are in good agreement with those reported by Benz *et al.* using X-ray diffraction data for the loose unsintered powder material (a = 0.37397(3) nm, b = 0.33082(2) nm, c = 1.23335(7) nm), a being within 0.03%, b within 0.34%, and c within 0.05% [6].

The Cr lattice parameter of 2.891(2) Å measured by neutron diffraction in this study is 0.007 Å larger than the value of 2.884 Å reported for pure Cr reported in the literature. The expanded lattice parameter suggests that there may be a small amount of nitrogen interstitial defects in the Cr phase. According to the Cr-N phase diagram, up to 1.7 at. % N can dissolve in Cr at the synthesis temperature of 1723 K [22]. Carbon or oxygen impurities may also contribute towards the larger than expected Cr phase lattice parameter.

The UO_2 lattice parameter of 0.5487(3) nm from the neutron data is higher than the literature value of 0.547127(8) nm reported for stoichiometric UO_2 [23]. As reported by Cardinaels et al. [24], the incorporation of Cr in UO_2 causes a reduction in the lattice parameter from 0.547109 nm for pure UO_2 to 0.546993 nm for UO_2 with a Cr content of 990 μg/g. Therefore, the lattice expansion observed for UO_2 here cannot be caused by Cr dissolution within the matrix. Moreover, oxide inclusions in the microstructure are a prerequisite for Cr dissolution and no UO_2 inclusions are observed via microscopy analysis.

Considering the lattice parameter behavior of non-stoichiometric UO_2 reported in literature ([25,26;27]), it can be observed that hyper stoichiometry, i.e., UO_{2+x}, also causes a decrease in the lattice parameter. The only cause for an increase in the UO_2 lattice parameter is the occurrence of oxygen vacancies in the hypo-stoichiometric regime, i.e., UO_{2-x}. Using the equation describing the dependence of lattice parameter with respect to oxygen stoichiometry reported by Bruneval et al. [27], the oxide phase in this work has a stoichiometry of $UO_{1.94(1)}$. Owing to the enlarged lattice parameter, the low phase fraction detected only in the neutron diffraction (2.1(4) wt.%) and absence of UO_2

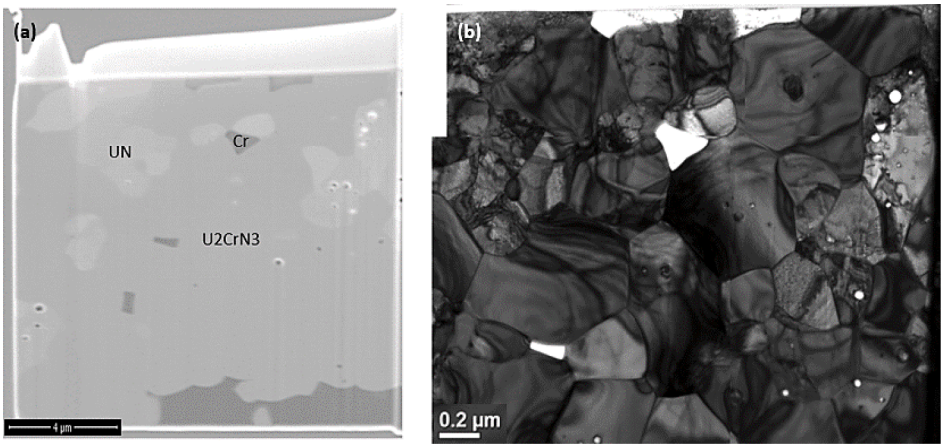

Fig. 6. (a) SEM and (b) BF-TEM image of the lamella.

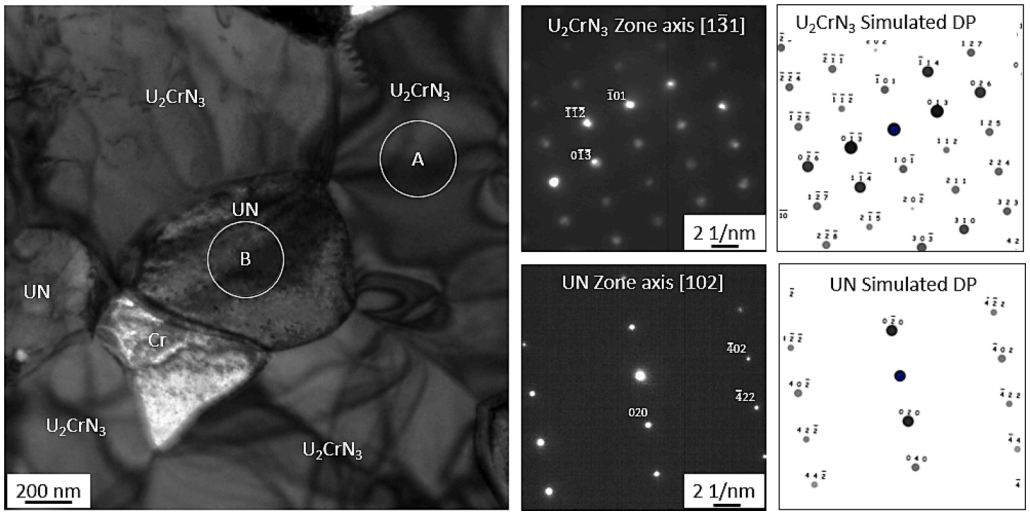

Fig. 7. BF-TEM micrograph and associated selected area electron diffraction patterns (DPs) from the U_2CrN_3 phase (A) and the UN phase (B). The respective simulated DPs are also presented.

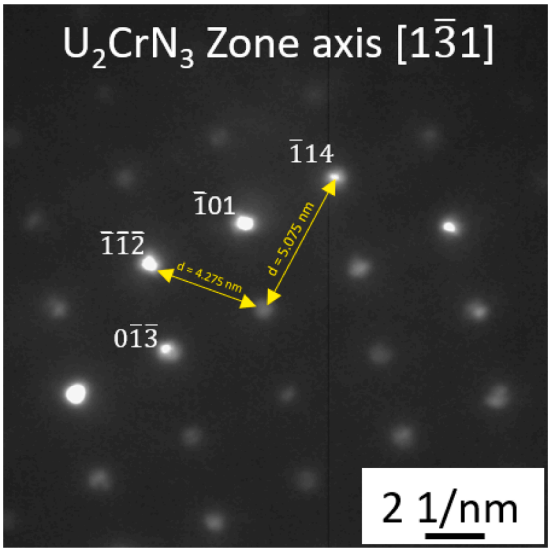

Fig. 8. SAED data showing in the ternary crystal structure.

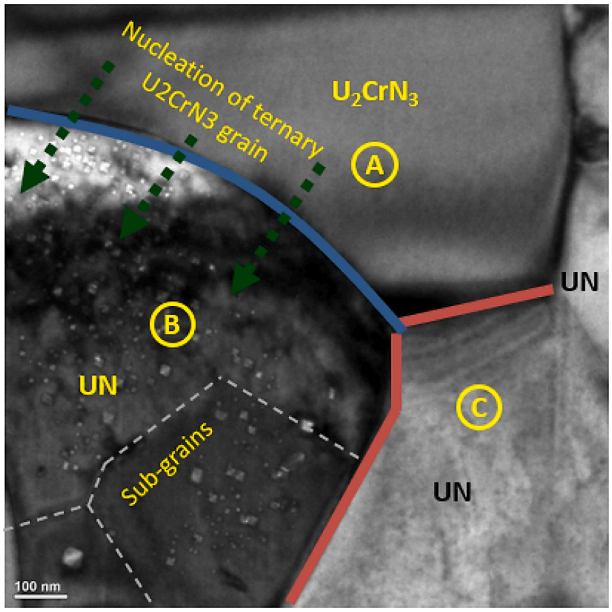

Fig. 9. TEM image showing concave boundary between UN and U_2CrN_3 grains.

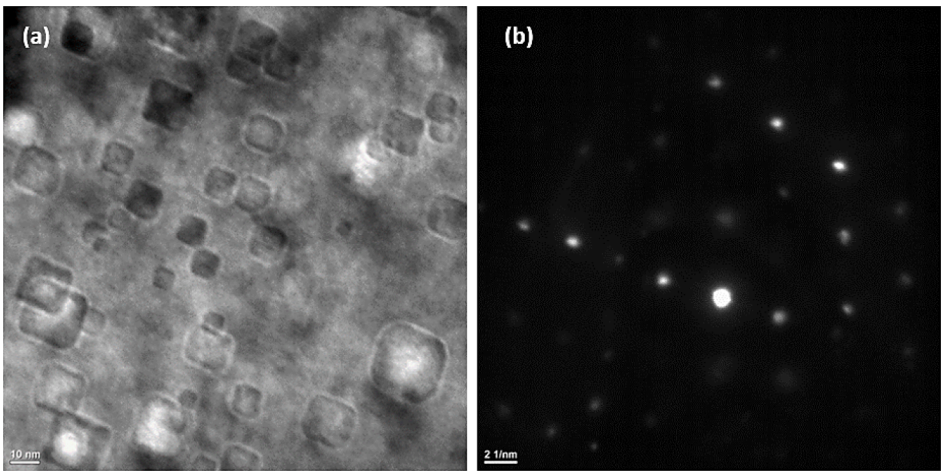

Fig. 10. (a) Nano domains near the UN and U_2CrN_3 grain boundary at high magnification (b) Diffuse diffraction pattern of nano domains.

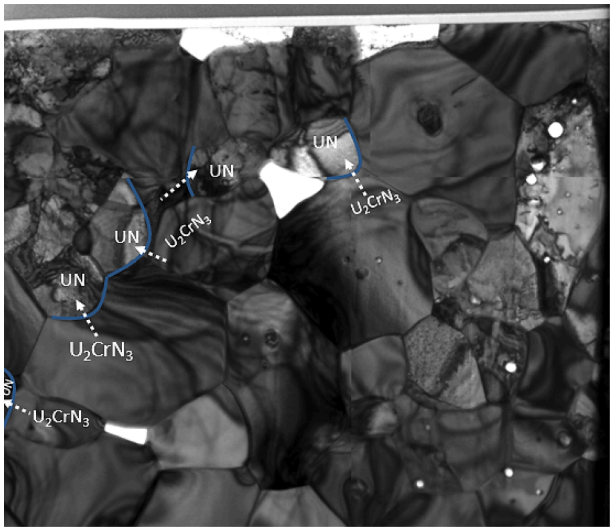

Fig. 11. BF-TEM image showing multiple sites of concave grain boundary of UN grains undergoing nucleation into the ternary phase. The UN/U_2CrN_3 grain boundary interface is marked by blue arcs and the white dashed arrows show the direction of nucleation. (For interpretation of the references to color in this figure legend, the reader is referred to the web version of this article.)

inclusions in the microstructure, it is therefore reasonable to assume that this hypo-stoichiometric oxide phase arises from surface oxidation during sample preparation and transfer for the neutron diffraction experiment.

Crystallographic details, including atomic positions and site occupancies of the U_2CrN_3 phase are not reliably known from the X-ray data. For X-ray diffraction, the scattering lengths of an atom are proportional to number of electrons or equivalently to Z, the atomic number. U_2CrN_3 contains low-Z N atoms, situated next to high-Z U atoms, meaning the N atoms have a small effect on the intensities observed. Consequently, the position of the N atoms at the 4*i* site (0, 0, z) had to be deduced theoretically by Benz *et al.* as approximately $z \sim a/2c = 0.151(3)$.

A key advantage of using neutrons to resolve structural information is that, unlike X-ray scattering lengths, neutron scattering lengths vary independently of atomic number. In the case of neutron scattering, it is the nucleus and not the electron cloud that interacts with the neutron

Table B1
Refinement details for the analysis of the U_2CrN_3-UN *Neutron Diffraction data.*

Diffractometer	Debye Scherrer
Radiation	Neutrons
Wavelength / nm	0.24131(3)
Absorption correction	0.1395
wRp / %	4.21
Goodness of fit	1.12

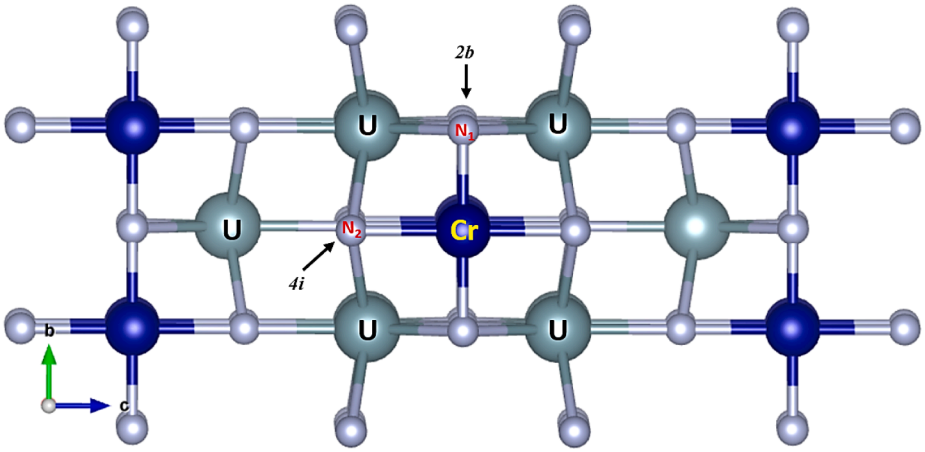

Fig. A1. Unit cell of U2CrN3 showing the two non-equivalent positions of nitrogen N_1 and N_2 at sites *2b* and *4i* respectively.

Table B2
Crystallographic parameters for the phases present in the U_2CrN_3-UN pellets as determined from Rietveld analysis of Neutron Diffraction data.

Phase	U_2CrN_3	UN	UO_2	Cr
Crystal system	Orthorhombic	Cubic	Cubic	Cubic
Space group	*Immm*	*Fm* $\bar{3}$ *m*	*Fm* $\bar{3}$ *m*	*Im* $\bar{3}$ *m*
Lattice parameters / nm	$a = 0.37388$ (2) $b = 0.33194$ (2) $c = 1.23393(7)$	$a = 0.48882$ (4)	$a = 0.5487$ (3)	$a = 0.2891$ (2)
Volume / nm^3	0.1531(1)	0.1168(1)	0.1652(3)	0.0242(1)
Formula units	2	4	4	2
Density / gcm^{-3}	12.36	14.33	10.86	7.14
Wt. fraction / %	54(8)	42(7)	2.1(4)	1.8(3)

Table B3
Crystallographic parameters for UN (42(7) wt.%; 38.2(1) vol.%) as determined from Rietveld analysis of the neutron diffraction data. Space group *Fm* $\bar{3}$ *m*, R_p = 3.39%, wR_p = 4.21%, a = 0.48882(4) nm.

Atom	Wyckoff	x	y	z	SOF[a]	Isotropic ADP[b] (pm^2)
U	4*a*	0	0	0	1.0	0.5(1)
N	4*b*	0.5	0.5	0.5	1.0	0.5(1)

[a] Site occupation factor.
[b] Isotropic atomic displacement parameters (U_{iso}).

Table B4
Crystallographic parameters for UO_2 (2.1(0.4) wt.%; 2.5(0.2) vol.%) used in the Rietveld analysis of neutron diffraction data. Space group Fm $\bar{3}$ m, R_p = 3.39%, wR_p = 4.21%, a = 0.5487(3) nm.

Atom	Wyckoff	x	y	z	SOF[a]	Isotropic ADP[b] (pm^2)
U	4*a*	0	0	0	1.0	1.0
O	8*c*	0.25	0.25	0.25	1.0	1.0

[a] Site occupation factor.
[b] Isotropic atomic displacement parameters (U_{iso}).

Table B5
Crystallographic parameters for Cr (1.8(0.3) wt.%; 3.26(0.1) vol.%) used in the Rietveld analysis of neutron diffraction data. Space group Im $\bar{3}$ m, R_p = 3.39%, wR_p = 4.21%, a = 0.2891(2) nm.

Atom	Wyckoff	x	y	z	SOF[a]	Isotropic ADP[b] (pm^2)
Cr	2*a*	0	0	0	1.0	1.0

[a] Site occupation factor.
[b] Isotropic atomic displacement parameters (U_{iso}).

beam. For U and N, the X-ray scattering lengths and coherent neutron scattering lengths vary by a factor of ~ 172 and ~ 1.24, respectively [13]. Therefore, neutron diffraction can be used to experimentally determine the crystallographic parameters (especially atomic positions and site occupation factors) of U_2CrN_3. Full structural details, derived from the neutron diffraction data for U_2CrN_3 are shown in Table 2 and can be found in the supporting crystallographic information framework (CIF) file.

Analysis of the neutron data shows that the N atoms at the 4*i* site are positioned closer to the Cr than previously suggested XRD results, resulting in more comparable Cr-N and U-N bond lengths in the U_2CrN_3 crystal structure as reported in Table 3. As a result, the refined structure of the U_2CrN_3 phase obtained from neutron diffraction varied from the starting model. Moreover, micro strain and crystalline size were determined to be similar in both UN and U_2CrN_3 phase.

Nano scale evaluation via transmission electron microscopy

Preliminary SEM imaging of the FIB lamella identifying the phases has been shown in Fig. 6**(a)**. The corresponding BF-TEM image showing the nano scale crystalline grain structure can be seen in Fig. 6**(b)**. Fig. 6 **(a)** shows that the lamella obtained has the three identified phases, with majority of the matrix being the ternary phase. However, it is also important to identify the interface of the ternary with the other phases to obtain complementary information about the crystallographic structure from TEM.

After identifying the phases, SAED data were retrieved to establish the crystallographic structure of U_2CrN_3 and pure UN phase. A BF-TEM micrograph displaying the three different phases found in the sample along with their SAED data is presented in Fig. 7. UN-SADP and U_2CrN_3-SADP were collected and indexed to confirm the crystal structure of UN and U_2CrN_3. The UN phase was indexed to the space group *Fm* $\bar{3}$ *m* while the U_2CrN_3 phase was indexed to the space group *Immm* in agreement with neutron diffraction analysis as discussed in **Section 3.2.** The simulated diffraction patterns calculated along the same zone axis directions for the two crystals are also presented in Fig. 7.

Spot distance (d) was obtained for the set of directions $< \bar{1}14 >$/ $<\bar{1}\bar{1}2>$ for the crystal structure of the ternary phase with reference to the central zone axis from the SAED data as shown in **(**Fig. 8**).** The resulting interplanar distance (1/d) was calculated to be 0.197 nm and 0.234 nm respectively for both planes. This is in good agreement with the shorter distances between the Cr-N bond than the U-N bond obtained from neutron diffraction in Section 3.2. Therefore, a correction in the description of the U_2CrN_3 structure phase is necessary.

Variation in the intensity of different diffraction spots can be seen in the U_2CrN_3-SAED data, while this could be attributed to a slight misalignment of the electron beam relative to the zone axis of the crystal lattice, some may arise from the structure.

In addition to the crystallographic information, an analysis of the interface between UN and the ternary phase was performed with the result shown in Fig. 9**.**

In Fig. 9, a concave grain boundary can be seen at the UN and U_2CrN_3 grain interface, marked by the blue curve, indicating that the larger ternary U_2CrN_3 grain, denoted "A" is growing into the neighboring smaller UN grain denoted "B". At this boundary significant nano defects within the sub grains (dashed gray lines) are observed, which may explain the absence of gradient in the composition of the sample, i.e., at any given location either only UN or only the ternary phase is present. The movement of grain boundaries (High Angle Grain Boundaries) and sub grain boundaries (Low Angle Grain Boundaries) mainly drive grain growth and nucleation respectively in crystalline materials occurring predominantly by the formation of nano domains of the ternary phase [28]. The direction of the transformation mechanism along the concave grain boundary is represented by dotted green arrows shown in Fig. 9**,** implicating the growth of the ternary into the neighboring UN grain. This inter-granular mechanism is known as grain growth and nucleation. This phenomenon typically occurs at grain boundaries when they have enough potential energy such that their diffusion coefficient is greater than the bulk grain providing easy route for grain growth and migration into the neighboring grain [29]. Such a nucleation mechanism occurring between U_2CrN_3, and UN grains infers the high purity of the starting UN powder and confirms the presence of negligible UO_2 in the crystal lattice.

It is interesting to note that the bottom UN grain (marked "C") does not have the grain boundary concavity, rather a "straight line" (red solid line) grain boundary, therefore there is no nucleation/growth at that site, and similarly, it also doesn't present nano defects. This signifies that grain boundary concavity between two grains exists only when the larger grain is about to grow into the neighboring smaller grain.

Interestingly, in the UN grain undergoing nucleation (marked "B" in Fig. 9), some intragranular nano domains are observed close to the

concave grain boundary between UN and U_2CrN_3 (marked by the blue curve) as seen in Fig. 9. At a higher magnification, these nano domains appear to have a distinct square or cube like shapes as shown in Fig. 10 **(a)**.

The overlapping cubes create a diffused scattering diffraction pattern as shown in Fig. 10**(b)**, in contrast to a sparse diffraction pattern for pure UN shown in Fig. 7. This incoherence of diffraction may arise from overlapping crystals in the lattice and could be related to the transformation mechanism occurring at the interface between U_2CrN_3 and UN, reinforcing the proposed formation mechanism in this study.

Several other regions of the crystalline structure also showed UN grains with similar concave grain boundaries surrounded by large ternary U_2CrN_3 grains as shown in Fig. 11. The concave grain boundaries between UN and U_2CrN_3 have been marked by blue arcs and the direction of nucleation is represented by dashed white arrows. This observation confirms the presence of multiple nucleation sites for the transformation of UN grains into the ternary phase in the crystal.

It is important to mention that the TEM study of the U_2CrN_3-UN pellet provided here configures a preliminary insight into the formation mechanism of the U_2CrN_3 ternary phase, possibly by grain nucleation of domains in UN matrix. However, more data is necessary to fully prove the formation mechanism that may not be entirely occurring from this phenomenon alone. More datapoints from statistical analyses, controls, sampling mechanism, and statistical reporting (e.g., P-values, CIs, effect sizes) is necessary and currently is out of scope for this work.

Conclusion

UN-20 vol%CrN (UN-9.5 wt% CrN) was studied in pellet form using neutron diffraction and microscopy. Studies of the bulk crystal structure and phase composition using neutron diffraction revealed the U_2CrN_3-UN pellets to comprise of 54(8) wt.% (56.04(1) vol.%) U_2CrN_3, 42(7) wt.% (38.2(1) vol.%) UN, 2.1(0.4) wt.% (2.5(0.2) vol.%) UO_2 and 1.8(0.3) wt.% (3.26(0.1) vol.%) Cr. For the first time, detailed crystallographic information for the U_2CrN_3 phase with space group *Immm* has been obtained using neutron data. The lattice parameters for U_2CrN_3 were found to be in excellent agreement with those previously reported using X-ray diffraction data and neutron data confirmed that all sites in U_2CrN_3 are fully occupied – an important conclusion given the impact of atomic number density on the neutronic calculations used in reactor core design. However, the results show that the N atoms at 4*i* sites are positioned more evenly between neighboring Cr and U atoms, giving rise to more comparable Cr-N and U-N bond lengths of 2.056(3) Å and 2.327 (4) Å, respectively. An accurate and in-depth description of the structure and composition of the U_2CrN_3-UN pellets is a key first step towards understanding the materials structure–function relationships. For nanoscale analysis of these pellets, TEM was employed to study the crystallographic structure of the U_2CrN_3 phase. TEM analysis showed the occurrence of grain nucleation during the transformation of UN into the ternary phase via formation of nano domains of the U_2CrN_3 phase in prior UN grains causing concave grain boundary interface between the two grains. Higher magnification TEM analysis revealed the presence of overlapping crystals in the lattice near the concave grain boundaries resulting in diffuse electron diffraction patterns supporting the ordered domain formation mechanism. Electron diffraction data provided comparable interplanar distances to those obtained from neutron diffraction, confirm the shorter distance for N-Cr than previously reported. This characterization study provides the basis for analysis of general physical properties needed to verify the suitability of application of U_2CrN_3-UN pellet as an advanced accident tolerant fuel.

CRediT authorship contribution statement

Sobhan Patnaik: Conceptualization, Methodology, Formal analysis, Investigation, Validation, Writing – original draft. **Yulia Mishchenko:** Formal analysis, Investigation, Writing – review & editing. **Jennifer H. Stansby:** Methodology, Formal analysis, Data curation, Investigation, Writing - original draft. **Andrea Fazi:** Formal analysis, Writing – review & editing. **Vanessa K. Peterson:** Supervision, Writing – review & editing. **Daniel Jädernäs:** Supervision, Writing – review & editing. **Mattias Thuvander:** Supervision, Writing – review & editing. **Kyle D. Johnson:** Supervision, Writing – review & editing. **Edward G. Obbard:** Supervision, Writing – review & editing. **Denise A. Lopes:** Supervision, Conceptualization, Validation, Methodology, Visualization, Formal analysis, Writing – review & editing.

Declaration of Competing Interest

The authors declare that they have no known competing financial interests or personal relationships that could have appeared to influence the work reported in this paper.

Data availability

Data will be made available on request.

Acknowledgments

Financial support for carrying out this research from The Swedish Strategic Research Foundation (SSF) within the SAFETY-project is gratefully acknowledged by the authors. We are thankful to Mirva Eriksson from the National Spark Plasma Sintering (SPS) facility at Stockholm University, Gunilla Herting from the Division of Surface and Corrosion Science at KTH. The authors also wish to acknowledge that TEM analysis was conducted at Chalmers Materials Laboratory (CMAL) at Chalmers University of Technology.

Appendix A. .

See Fig. A1.

Appendix B. Neutron diffraction supporting information

See Table B1, Table B2, Table B3, Table B4, Table B5,

References

[1] IEA, Nuclear Power in a Clean Energy System, IEA, Paris, 2019 (accessed 16th June 2022.
[2] J.K. Watkins, et al., Challenges and opportunities to alloyed and composite fuel architectures to mitigate high uranium density fuel oxidation: Uranium mononitride, J. Nucl. Mater. 553 (2021), 153048.
[3] Y. Mishchenko, K.D. Johnson, A. Claisse, J. Wallenius, D.A. Lopes, Design and fabrication of UN composites: from first principles to pellet production, J. Nucl. Mater. (2021), https://doi.org/10.1016/j.jnucmat.2021.153047, 153047 May.
[4] Aditya P. Shivprasad, Amber C. Telles, Joshua T. White, Report on waterproofing of UN studies, in: Prepared for U.S. Department of Energy FCRD Program, Los Alamos National Laboratory, August 22, 2019, NTRD-M2FT-19LA020201021, LA-UR-19-28422.
[5] Y. Mishchenko, et al., Potential accident tolerant fuel candidate: Investigation of physical properties of the ternary phase U_2CrN_3, J. Nucl. Mater. 568 (September 2022), 153851.
[6] R. Benz, W.H. Zachariasen, Crystal structures of Th2CrN3, Th2MnN3, U_2CrN_3 and U2MnN3, J. Nucl. Mater. 37 (1) (1970) 109–113.
[7] R.E. Rundle, et al., The Structures of the Carbides, Nitrides and Oxides of Uranium, J. Am. Chem. Soc. 70 (1) (1948) 99–105.
[8] P. Malkki, M. Jolkkonen, T. Hollmer, J. Wallenius, Manufacture of fully dense uranium nitride pellets using hydride derived powders with spark plasma sintering, J. Nucl. Mater. 452 (1) (2014) 548-551 Sep., doi: 10.1016/j.jnucmat.2014.06.012.
[9] Y. Mishchenko, K.D. Johnson, D. Jädernäs, J. Wallenius, D.A. Lopes, Uranium nitride advanced fuel: an evaluation of the oxidation resistance of coated and doped grains, J. Nucl. Mater. 556 (2021) 153249 Dec., doi: 10.1016/j.jnucmat.2021.153249.
[10] A.J. Studer, M.E. Hagen, T.J. Noakes, Wombat: The high-intensity powder diffractometer at the OPAL reactor, Phys. B Condens. Matter 385–386 (2006) 1013–1015.

[11] Sample Environment Equipment Handbook, Australian Centre for Neutron Scattering, Australian Nuclear Science and Technology Organization, June 23, 2021 (Vers. 1.50), Australian Government, ANSTO.
[12] J.M. Hudspeth, Short-Range Order in Ferroelectric Triglycine Sulphate, Australia National University, October 2012. PhD Thesis,.
[13] D.R. Black, et al., Certification of standard reference material 660B, Powder Diffr. 26 (2) (2011) 155–158.
[14] B.H. Toby, R.B. von Dreele, GSAS-II: the genesis of a modern open-source all purpose crystallography software package, J. Appl. Cryst. 46 (2) (2013) 544–549.
[15] Neutron Activation and Scattering Calculator [Accessed 31 June 2022]. Available from: https://www.ncnr.nist.gov/resources/activation/.
[16] R.M. Langford, M. Rogers, In situ lift-out: Steps to improve yield and a comparison with other FIB TEM sample preparation techniques, Micron 39 (2008) 1325–1330, https://doi.org/10.1016/j.micron.2008.02.006.
[17] A. Jain, S.P. Ong, G. Hautier, W. Chen, W.D. Richards, S. Dacek, S. Cholia, D. Gunter, D. Skinner, G. Ceder, K.A. Persson, Commentary: The materials project: A materials genome approach to accelerating materials innovation, APL Mater. 1 (2013), 011002, https://doi.org/10.1063/1.4812323.
[18] Basic image analysis and manipulation in Image, J. Hartig, Curr. Protoc. Mol. Biol., Vol. 102 (1) (2013), pp. 14.15.1-14.15.12, 10.1002/0471142727.mb1415s102p.
[19] H. E. Swanson, et al., Standard X-Ray Diffraction Powder Patterns, National Bureau of Standards Monograph 25 — Section 5 Issued August 31, 1967.
[20] L. Desgranges, G. Baldinozzi, G. Rousseau, J.-C. Niepce, G. Calvarin, Neutron Diffraction Study of the in Situ Oxidation of UO2, Inorg. Chem. 48 (2009) 7585–7592, https://doi.org/10.1021/ic9000889.
[21] P. Karen, E. Suard, F. Fauth, Crystal Structure of Stoichiometric YBa2Fe3O8, Inorg. Chem. 44 (2005) 8170–8172.
[22] J.W. Seok, N.M. Jadeed, R.Y. Lin, Sputter-deposited nanocrystalline Cr and CrN coatings on steels, Surf. Coat. Technol. 138 (1) (2001) 14–22, https://doi.org/10.1016/S0257-8972(00)01120-8. ISSN 0257–8972,.
[23] G. Leinders, T. Cardinaels, K. Binnemans, M. Verwerft, Accurate lattice parameter measurements of stoichiometric uranium dioxide, J. Nucl. Mater. 459 (2015) 135–142, https://doi.org/10.1016/j.jnucmat.2015.01.029. ISSN 0022–3115,.
[24] T. Cardinaels, K. Govers, B. Vos, S. Van den Berghe, M. Verwerft, L. de Tollenaere, G. Maier, C. Delafoy, Chromia doped UO2 fuel: Investigation of the lattice parameter, J. Nucl. Mater. 424 (1–3) (2012) 252–260, https://doi.org/10.1016/j.jnucmat.2012.02.025. ISSN 0022–3115,.
[25] Masato Kato, Kenji Konashi, Lattice parameters of (U, Pu, Am, Np)O2−x, Journal of Nuclear Materials, Volume 385, Issue 1, 2009, Pages 117-121, ISSN 0022-3115, Doi: 10.1016/j.jnucmat.2008.09.037.
[26] Lahmer Lynds, W.A. Young, J.S. Mohl, G.G. Libowitz, X-Ray and Density Study of Nonstoichiometry in Uranium Oxides, Nonstoichiometric Compounds. January 1, 1963, pp. 58-65, DOI:10.1021/ba-1964-0039.ch005.
[27] F. Bruneval, M. Freyss, J.-P. Crocombette, Lattice constant in nonstoichiometric uranium dioxide from first principles, Phys. Rev. Materials 2 (2) (February 2018).
[28] F.J. Humphreys, M. Hatherly, Chapter 5 - The Mobility and Migration of Boundaries, in: F.J. Humphreys, M. Hatherly, Recrystallization and Related Annealing Phenomena (Second Edition), Elsevier, 2004, pp. 121-167, ISBN 9780080441641, Doi: 10.1016/B978-008044164-1/50009-8.
[29] A. Banos, N.J. Harker, T.B. Scott, A review of uranium corrosion by hydrogen and the formation of uranium hydride, Corros. Sci. 136 (2018) 129–147.